Enhancing the structural, optical and electrical properties of ZnO nanopowders through (Al + Mn) doping

C. Belkhaoui, N. Mzabi, H. Smaoui, P. Daniel

HAL Id: hal-02143726

https://univ-lemans.hal.science/hal-02143726

Submitted on 21 Oct 2021

Enhancing the structural, optical and electrical properties of ZnO nanopowders through (Al+Mn) doping

Chedia Belkhaoui, Nissaf Mzabi, Hichem Smaoui and Philippe Daniel

Unité de recherche physique des matériaux isolants et semi isolants, Faculté des Sciences de Sfax, B. P. 1171, 3000 Sfax, Tunisia.

Université du Maine, Institut des Molécules et Matériaux du Mans, UMR CNRS 6283, Avenue Olivier Messiaen, 72085, Le Mans Cedex 9, France.

Abstract

Undoped ZnO and $Zn_{0.97-x}Al_{0.03}Mn_xO$ (x = 0, 1, 2 and 3%) nanopowders (NPs) were synthesized by co-precipitation method. They were characterized by X-ray diffraction (XRD), Fourier transformed infrared (FTIR), Raman, UV-visible, photoluminescence (PL) and impedance spectroscopies. All samples exhibit a single phase wurtzite type. The average crystallite size lying between 22 and 42 nm was found to increase for all doped ZnO samples. The optical transmission in the visible region was improved due to doping. The optical band gap is in the range of 3-3.4 eV and was found to decrease up to 2% of Mn content but slightly increases with further doping. All PL spectra exhibit two emission peaks in UV and visible regions. The deconvolution of the visible emission peak reveals different emissions for all samples. An additional yellow emission is noticed for (Al+Mn) ZnO doped samples suggesting that the incorporation of aluminum and manganese in the zinc oxide host lattice enhances luminescence properties of ZnO. The ac conductivity (σ_{ac}) was found to follow Jonscher's power law and was improved with doping. Cole-Cole plots of all samples were

suitably fitted to a circuit consisting in a parallel combination of a resistance and a constant phase element (CPE).

1. Introduction

The zinc oxide (ZnO) has received considerable attention from researchers owing to its interesting properties and numerous applications. It shows a large band gap (3.37 eV) and an elevated exciton binding energy (60 meV) at room temperature [1], a high piezoelectric constant [2] and high chemical stability [3]. Its interesting properties make it a promising material for a wide range of applications such as ultraviolet light-emitting diodes, photodetectors, solar cells, spintronic devices, biological sensors and photo catalysts [3,4, 5,6].

Different methods have been used to synthesize ZnO nanostructures like co-precipitation method [7], spray pyrolysis technique [8], sol-gel method [9], pulsed laser deposition [10], hydrothermal method [11,12,13,14], solid state reaction technique [15] and wet chemical method [16]. The co-precipitation method which is a simple, low cost and effective synthesized method was used in the present work for synthesizing undoped and doped ZnO nanopowders.

Doping can be an efficient means for improving physical properties, especially optical and electrical ones or tuning them to suit specific needs and applications. For example, the optical and electrical properties of ZnO can be improved upon doping with Group III elements such as Aluminum (Al), Gallium (Ga) and Indium (In) [17]. Li et al. [18] have reported that the incorporation of aluminium in ZnO can significantly enhance its dielectric constant. It was found that the electrical conductivity of ZnO can be proved by Al doping [19]. Transition

metal (TM) doped ZnO nanoparticles are promising candidates for a variety of applications. Among the TM dopants, manganese (Mn) is a suitable one for the incorporation into the ZnO lattice due to its high solubility with respect to ZnO [20]. Several researches have dealt with the study of manganese doping effects on different properties of ZnO [21-23]. Hence there are researches reported on properties of Al and Mn doped ZnO nanostructures. However, to the our knowledge there is no published paper devoted to structural, optical and dielectric properties of (Al+Mn) doped ZnO nanopowders synthesized by the co-precipitation method.

In this study, undoped, Al and (Al+Mn) doped ZnO nanopowders were elaborated using the co-precipitation process. The effects of doping on structural, optical, dielectric and conducting properties of ZnO nanopowders were studied in detail.

2. Experimental

2.1. Nanopowders synthesis

Undoped ZnO and $Zn_{1-x}Al_{0.03}Mn_xO$ (x = 0.00 (AlMnZ0), 0.01 (AlMnZ1), 0.02 (AlMnZ2) and 0.03 (AlMnZ3)) nanopowders have been elaborated through the chemical co-precipitation process. The host precursor is zinc chloride tetrahydrate ($ZnCl_2.4H_2O$) while the doping ones are manganese chloride hexahydrate ($MnCl_2.6H_2O$] and aluminium chloride tetrahydrate ($AlCl_3.4H_2O$). For synthesizing the undoped ZnO nanopowder, an appropriate amount of $ZnCl_2$ was dissolved in a mixture of distilled water and absolute ethanol at room temperature under a magnetic stirring for 30 min. Then, aqueous NaOH solution was added drop by drop to the starting solution until the pH reached the value 10. The obtained solution was magnetically stirred for 90 min and the precipitation occurred. The precipitate was separated from the solution by filtration and washed several times with distilled water. Afterwards, it was oven-dried for 15 h at 120°C. The resulting powder was then calcined for 4 hours at 500°C. All samples were synthesized using the same process.

2.2. Experimental techniques

Crystal structures of undoped, Al and (Al+Mn) doped ZnO nanopwders were analyzed by means of Bruker D8 Advanced X-ray diffractometer with $Cu\ K\alpha$ radiation ($\lambda = 1.54056$ Å) for 2θ varying from 20 to 75°. Fourier transformed infrared (FTIR) analysis was carried out using Perkin Elmer–spectrometer in the wavenumber range of 4000-400 cm^{-1}. Raman scattering spectral measurements were performed in the range of 50-900 cm^{-1} by means of a T-64000 Raman spectrometer (Horiba-Jobin-Yvon) using the 514.5 nm radiation of an Ar/Kr laser as excitation. Optical absorbance and transmittance measurements were performed with an UV-VIS spectrophotometer (optizen POP) in the 200-1000 nm wavelength range. The photoluminescence spectra were recorded at room temperature in a wavelength range of 300-750 nm using a Perkin Elmer LS-55 fluorescence spectrometer with a 325 nm wavelength excitation. Impedance measurements were performed on a Solartron SI1260 Impedance Gain-Phase analyzer in the frequency range of 50 Hz-5 MHz. All measurements were performed at room temperature.

3. Results and discussion

3.1. Powder X-ray diffraction

X-ray diffractogram of undoped, Al and (Al+Mn) doped ZnO nanopowders are depicted in **Fig. 1**. All diffraction peaks are indexed to the ZnO wurtzite structure according to the standard data (JCPDS card No. 36-1451). As no secondary or impurity phases were revealed, it is suggested that Mn^{2+} and Al^{3+} ions were substituted into Zn^{2+} ion sites or incorporated into interstitial sites in the lattice without altering the hexagonal wurtzite structure of ZnO **[24]**. The lattice parameters (a,c) and the volume of unit cell (v) of all samples were calculated using the following formulae **[3,25]**:

$$a = \frac{\lambda}{\sqrt{3}sin\theta_{(100)}} \tag{1}$$

$$c = \frac{\lambda}{sin\theta_{(002)}} \tag{2}$$

$$V = \frac{\sqrt{3}a^2 c}{2} = 0.866a^2 c \tag{3}$$

where λ is the wavelength of the $CuK\alpha$ radiation (1.54056 Å) and θ is the Bragg angle. The values of the structural parameters are listed in **table 1**. The 'c' value of undoped ZnO sample is smaller than the standard value (5.2066 Å), which may be due to the presence of oxygen vacancies [20]. As shown in **table 1**, a and c parameters are doping dependent. Indeed, the defects generated by the foreign atoms as well as the difference in ionic radii of the dopants compared to those of the substituted matrix, influence the semiconductor lattice parameters [26]. The increment of lattice parameters (a, c) under aluminium doping effect can be interpreted by the incorporation of Al^{3+} ions into interstitial positions in the host lattice as it has been previously reported [27,28]. The addition of Mn content increases a and c parameters as a result of the substitution of Zn^{2+} ions with radii of 0.74 Å by Mn^{2+} ones with higher radii (0.83 Å) [2,29]. The gradual substitution of Zn^{2+} ions by Mn^{2+} ones is likely the cause of the lattice parameters increment with increasing Mn content up to 2%.

The Zn−O bond length (l) was determined for all samples using this relation [2]:

$$l = \sqrt{\frac{a^2}{3} + \left(\frac{1}{2} - u\right)^2 c^2} \tag{4}$$

where u is a positional parameter given by [26]:

$$u = \frac{a^2}{3c^2} + 0.25 \tag{5}$$

The observed increase of Zn−O bond length for Al and (Al+Mn) doped ZnO NPs (**table 1**) confirms the incorporation of dopant ions in the zinc oxide host lattice [26].

The micro-strain (ε_z) along the c-axis was calculated using the following formula [3]:

$$\varepsilon_z = \frac{c - c_0}{c_0} \tag{6}$$

where c and c_0 (5.2066 Å) are the calculated and standard lattice constant parameters respectively [30].

The calculated ε_z values are given in **table 1**. It is remarkable that the micro-strain was found to be compressive for undoped and Al doped ZnO samples. The (Al+Mn) doping causes a changeover from compressive strain to tensile one. The ε_z magnitude increases with increasing Mn content until 2% and decreases for 3%. This may be due to the fact that the incorporated dopant ions are trapped in non-equilibrium positions initially up to a certain Mn content (here it is 2%) and with further doping content, Mn^{2+} ions could have shifted to equilibrium positions, which could release the tensile strain [3].

The texture coefficient ($TC_{(hkl)}$) values which correspond to the prominent diffraction peaks were determined from the X-ray data using this relation [31,32]:

$$TC_{(hkl)} = \frac{I_{(hkl)}/I_{0(hkl)}}{\frac{1}{N}\sum I_{(hkl)}/I_{0(hkl)}} \tag{7}$$

where $I_{(hkl)}$ is the measured XRD peak intensity, $I_{0(hkl)}$ is the standard intensity corresponding to the same plane, taken from the JCPDS data card No. 36-1451 and N is the number of the considered diffraction peaks. $TC_{(hkl)}$ variations versus composition are displayed in **Fig. 2**. It is evident from this figure that Al and (Al+Mn) doping induce a change in the preferential crystalline orientation from the one along (002) plane to the other along (100) plane whose predominance degree decreases with increasing Mn content. The change in the type of strain as well as its magnitude may be the main reason for the variation in the orientation of crystallites as reported by Snega et al. [31].

The average crystallite size (D) and the micro-strain (ε) were determined according to the Williamson-Hall (W-H) model [33]:

$$\beta cos\theta = \frac{K\lambda}{D} + 4\,\varepsilon\sin\theta \tag{8}$$

where β is the full width at half maximum (FWHM) of the peak, θ is the Bragg's diffraction angle, K is the shape factor ($K = 0.9$), λ is the wavelength X-ray diffraction ($\lambda = 1.54056\,\text{Å}$ for $CuK\alpha$ radiation).

The X-ray diffraction peak broadening is due to both instrumental and sample related effects. Before estimating the crystallite size and lattice strain, it is necessary to correct the instrumental effect. The instrumental corrected broadening β of each diffraction peak is estimated using the following relation [25]:

$$\beta = \sqrt{\beta_{measured}^2 - \beta_{instrumental}^2} \tag{9}$$

where $\beta_{measured}$ is the measured broadening while $\beta_{instrumental}$ is the broadening due to the instrumental contribution.

The plots of $\beta cos\theta$ versus $4sin\theta$ for undoped, Al and (Al+Mn) doped ZnO samples (**Fig. 3**) were fitted according to equation (8). For each sample, the average crystallite size (D) was estimated from the y-intercept of the corresponding linear fit extrapolation and the strain (ε) is given by the slope of this fit. The dislocation density (δ) was calculated for all samples by the following formula [34]:

$$\delta = \frac{1}{D^2} \tag{10}$$

Values of D, ε and δ are gathered in **table 1.** Their variations as a function of composition are presented in **Fig. 4**. As shown in this figure, the average crystallite size for all doped NPs is larger than that for undoped one, which indicates the improvement of crystalline quality. It increases with the rise in Mn content until 2% and decreases for 3%. The D increment can be related to the expansion of lattice volume due to the increase of bond length [2] while its decrease may be linked to the Zener pinning [35]. Indeed, for 3% of Mn content, the retarding force generated by lattice defects may be higher than the driving one causing the outward movement of the grain boundaries, therefore the particles cannot grow any longer [36]. The dependence of the strain and the dislocation density upon composition (**Fig. 4**) shows that all doped samples have lower ε and δ values as compared to undoped ZnO sample. This finding

confirms the improvement of crystalline quality due to doping. According to the D, ε and δ value variations (**Fig. 4**), the AlMnZ2 nanopowder presents the better crystalline quality.

3.2. Morphological analysis

The surface morphologies of undoped, Al and (Al+Mn) doped ZnO nanopowders were shown in **Fig. 5 (a-d)**. The SEM micrographs reveal the presence of a large aggregate of smaller spherical nanoparticles. The particle size increased with the increase in Mn content. This is consistent with the crystallite size obtained from XRD patterns. From these images, it is observed that undoped sample consists of irregularly shaped and loosely packed particles with the average particle size in the range of 30–40 nm. The particle size increases drastically when the dopants are added (80-125 nm). Agglomerated spherical crystallites are observed in all the Mn doped samples.

3.3. Fourier transformed infrared (FTIR) analysis

The chemical structures of undoped, Al and (Al+Mn) doped ZnO nanopowders were examined by Fourier transformed infrared spectroscopy. FTIR spectra of all samples are depicted in **Fig. 6**. The band appearing around 3500 cm^{-1} is characteristic of O−H stretching vibration [37,38] while the other one observed around 1620 cm^{-1} is assigned to H−O−H bending vibration [39]. These bands arise from a small amount of H_2O existing on the surface of ZnO nanocrystalline, which may be due to moisture [39,40]. For all doped ZnO samples, the ν(O−H) band intensity was increased and the shoulders (around 3560 cm^{-1} and 3450 cm^{-1}) become more pronounced as compared to undoped ZnO sample. This finding suggests the increase of hydroxyl groups amount due to increased water adsorption resulting from the increase in the content of surface defects [41]. Indeed, for metal oxides, the concentration of hydroxyl groups reflects the concentration of surface defects particularly anion vacancies [42]. The hydroxyl groups with negative charges are attached to the surface defects having

positive charges like oxygen vacancies in metal oxides. Consequently, the concentration of surface defects can be indirectly inferred from the intensities of stretching vibrations of hydroxyl groups [42]. The band appearing around 496 cm^{-1} on IR spectrum of undoped ZnO sample is ascribed to stretching mode of Zn−O bonding [31,43]. It was found to be shifted towards higher wave number side for all ZnO doped NPs. The change in the vibrational frequency can be due to the perturbation of Zn-O bonding and the difference in the bond lengths as a result of the incorporation of dopants ions in the ZnO host lattice [3,40,44,45].

3.4. Raman analysis

Raman spectroscopy is an effective technique for detecting the incorporation of dopants, defects and disorder in a host lattice [26,46]. Raman scattering experiments were performed on all samples to reveal the structural changes in ZnO host lattice, induced by Al and (Al+Mn) doping. At the Γ point of the Brillouin zone, the optical vibration modes relative to the hexagonal Wurtzite ZnO structure (P6$_3$mc) [47] are represented by [48]: $\Gamma_{opt} = A_1 + E_1 + 2E_2 + 2B_1$.

The B_1 modes are known as silent modes since they are inactive in Raman scattering. The A_1 and E_1 modes are polar and both infrared and Raman active while E_2 modes are non polar but Raman active. The non-polar E_2 modes have two frequencies namely E_{2H} (high) and E_{2L} (low) related to the motion of oxygen and zinc sub lattice respectively [49,50]. Strong E_{2H} (high) mode is characteristic of the wurtzite lattice and indicates good cristallinity. Raman scattering spectra of undoped, Al and (Al+Mn) doped ZnO NPs are depicted in **Fig. 7**. The observed sharp peak around $439 \ cm^{-1}$ on the spectrum of undoped ZnO sample is assigned to E_{2H} optical phonon mode corresponding to the band characteristic of wurtzite phase of ZnO [51,52]. The presence of this mode on Raman spectra of all doped ZnO samples confirms the unaffected hexagonal wurtzite structure with doping. Furthermore, the shifting of E_{2H} peak toward lower frequency side and the decrease of its intensity for 2% of Mn content

are due to structural defects and local lattice distortions induced by doping [53]. The Raman modes located around 115 and 232 cm^{-1} are attributed to E_{2L} and $2E_{2L}$ modes respectively [54]. The weak broad peak appearing around 571 cm^{-1} is assigned to A_1 longitudinal optical mode (LO) which arises by defects such as O-vacancy, Zn-interstitial defect or their complexes [44,55,56]. The intensity of this peak increases with doping and principally for 2% of Mn content indicating an increase in defects amount within doped samples. This result is consistent with PL study which will be presented later. The peak around 541 cm^{-1} indicated by an arrow, is also raised because of the lattice disorder and defects [57]. Moreover, the Raman spectra of (Al+Mn) doped ZnO samples display each one an additional peak around 670 cm^{-1} attributed to the vibration mode of Mn-O [57-59], which confirms the substitution of Mn^{2+} ions in Zn^{2+} sites and then the incorporation of Mn dopant in the ZnO host lattice as revealed by XRD analysis and confirmed by the-FTIR results.

3.5. Study of optical properties

3.5.1. Absorption and transmission spectra

The absorption spectra of undoped, Al and (Al+Mn) doped ZnO nanopowders are displayed in **Fig. 8**. It is clear from this figure that the optical absorption decreases due to doping and varies with increasing Mn content. The transmission spectra of all samples (**Fig. 9**) show almost an opposite trend of the absorption spectra. The observed increase of transmittance in visible range due to doping may be associated with the decrease in light scattering at less grain boundaries [60,61] as the average crystallite size increased. The disorder in the doped ZnO samples may be another factor that accounts on transmittance enhancement [62]. The transmittance was found to increase with increasing Mn content up to 2% then it decreases with further rise in doping content. This transmittance variation can be related to the change in average crystallite size (size effect) and disorder with increasing Mn content.

3.5.2. Optical band gap and Urbach energies

The optical band gap (E_g) for all nanopowders was evaluated using the Tauc relationship given as follows [63]:

$$\alpha h\nu = B(h\nu - E_g)^n \tag{11}$$

where α is the absorption coefficient ($\alpha = 2.303A/d$ with A is the absorbance and d is the thickness of the cuvett), B is a constant and $h\nu$ is the photon energy. The value of n depends on the nature of the electronic transition responsible for absorption [63,64]. It is equal to $1/2$ for ZnO which is a direct band gap semiconductor [63,65]. The optical band gap could be obtained by extrapolating the linear portion of the $(\alpha h\nu)^2$ versus $h\nu$ plot (Tauc's plot) to $h\nu$ axis.

Tauc's plots of all nanopowders are shown in **Fig. 10** while the variation of E_g as a function of composition is given in **Fig. 11**. The optical band gap was found to be 3.37 eV for the undoped ZnO nanopowder and 3.12 eV for the Al doped one (**table 2**), indicating a decrease of E_g value due to Al doping. Similar E_g value behavior was reported in other researches [28, 66,67]. The band gap narrowing may be due to doping induced band edge bending [67] and also the average crystallite size increase [2,68]. For (Al+Mn) doped ZnO nanopowders, the band gap decreases with increasing Mn content until 2% and increases for 3%. The band gap shrinkage may originate from the strong $s - d$ and $p - d$ exchange interaction between the band electrons of ZnO and the localized 'd' electrons of the Mn^{2+} ions substituting Zn^{2+} ones [3,69]. Bylsma et al. [70] have theoretically explained the E_g narrowing under the $sp - d$ exchange interaction effect. The higher defects amount may be an another cause contributing to the E_g decrease [32]. The observed E_g blue shift for 3% of Mn doping may be interpreted in terms of the average crystallite size decrease [2] and also Burstein-Moss effect [71]. For this effect, Fermi level shifts inside the conduction band because of the increase of electron carrier concentration. As the states below such shifting in the conduction band are populated,

the absorption edge is pushed to higher energies, leading to larger optical band gap for 3% of Mn doping [69].

The incorporation of impurity into a semiconductor often results in the formation of band tailing [72]. The band tail energy or Urbach energy (E_u) which is considered to be a measure of disorder degree [73] and characterizes the local defects, follows the empirical Urbach law [32, 62]:

$$
\begin{cases}
\alpha(h\nu) = \alpha_0 \exp\left(\dfrac{h\nu}{E_u}\right) & (12) \\
E_u = h\left[\dfrac{d(ln\alpha(h\nu))}{d\nu}\right]^{-1} & (13)
\end{cases}
$$

where α_0 is a constant.

The Urbach energy was estimated by plotting $ln\alpha$ versus $h\nu$ and fitting the linear portion of the curve with a straight line. Its value is given by the slope inverse of the linear portion. E_u values for all samples are listed in **table 2** while the E_u variation as a function of composition is plotted in **Fig. 11**. As shown in this figure, the Urbach energy increases as the Mn content increases from 0 to 2 % and then decreases for 3 %. This finding suggests a variation of disorder and defects content depending on Mn doping content. Furthermore, the composition dependence of Urbach energy exhibits an opposite behavior as compared to that of optical band gap which confirms the close relationship between these two parameters. This indicates that the change in optical band gap is related to the disorder variation [74,75].

3.5.3. Photoluminescence (PL) study

The PL spectroscopy is an effective tool for examining the existence of defects in semiconductors. The room temperature PL spectra of undoped, Al and (Al+Mn) doped ZnO nanopowders (**Fig. 12**) exhibits each one two emission peaks in UV and visible regions. The UV emission peak, results from free excitonic radiative recombination corresponding to the near band edge (NBE) emission [76,77,78] whereas the wide visible one is related to

impurities and defects within the crystalline structure [79]. The peak associated whith the defect was found to be more intensive than that of undoped one. The rise in the defect contents after doping leads to an increase in radiative recombination centers which increases the defect content and therefore the corresponding defect peak intensity.

PL spectra were deconvoluted by the use of multi peak Gaussian function (**Fig. 13**). The position, energy and the corresponding attribution of each emission peak are given in **table 3**. The weak peak positioned around 385 nm corresponds to UV emission. It was gradually red shifted up to 2% of Mn content and blue shifted with further doping, which corroborates the observed E_g variation [62]. In the visible region, a violet emission peak is located around 400 nm for undoped sample and was found to be red shifted due to doping. It may be due to defects such as interface traps existing at the grain boundaries [80]. The deconvoluted PL spectrum of undoped ZnO sample shows a blue emission at 466 nm ascribed to the exciton recombination between the electron localized at the interstitial zinc (Zn_i) and the holes in valence band [32].Those of doped ZnO NPs exhibit each one a blue-green emission peak around 470 and 483 nm for Al and (Al+Mn) doping respectively, which may be assigned to electrons transition from the shallow donor levels of oxygen vacancies to the valence band [2,3]. The peak at around 562 nm appearing on PL spectra is attributed to the green-yellow emission [32]. It results from the recombination of electrons with holes trapped in singly ionized oxygen vacancies (V_0^+) [81]. The component peak around 600 nm only noticed for (Al+Mn) doped ZnO nanopowders corresponds to yellow emission [82] and may be associated with oxygen interstitials (O_i) [83]. This result indicates that the inclusion of manganese in ZnO lattice improves its luminescence properties in the visible domain.

3.6. Dielectric study

3.6.1. Dielectric constant and dielectric loss

The complex dielectric permittivity ε^* of a material is given by the following expression [16]:

$$\varepsilon^* = \varepsilon' - j\varepsilon'' \tag{14}$$

where the real part ε' describes the stored energy while the imaginary part ε'' describes the dissipated energy under applying an electric field.

The dielectric constant (ε'_r) is defined as the ratio of the real part of complex permittivity (ε') to the permittivity of free space ($\varepsilon_0 = 8.8542 \times 10^{-12} F.m^{-1}$).

Fig. 14 shows the variation of ε'_r as a function of frequency for undoped, Al and (Al+Mn) doped ZnO samples. All $\varepsilon'_r(f)$ plots exhibit at lower frequencies a rapid decrease which becomes slow with increasing frequency until an almost frequency independent behavior is reached at higher frequencies. The observed dielectric behavior can be explained in terms of Maxwell-Wagner interfacial model [84] and Koops phenomenological theory [85]. It is assumed that the dielectric medium is made of well conducting grains separated by resistive grain boundaries [86]. The charge carriers can easily move within the grains when an external electric field is applied but they are accumulated at the grain boundaries resulting in the interfacial polarization [87]. This process can produce large polarization and hence high dielectric constant at lower frequencies [37,88]. The observed ε'_r decrease with the rise in frequency is due to the fact that any species contributing to polarizability is found to show lagging behind the applied field at higher and higher frequencies [86]. Beyond a certain frequency, dipoles cannot follow the alternating field, as result a frequency independent dielectric behavior appears. Furthermore, at lower frequencies ε'_r increases with increasing Mn content and slightly exceeds that of the undoped ZnO sample at 3% of Mn doping.

Dielectric loss or loss tangent ($tan\delta = \varepsilon''/\varepsilon'$) is represented as dissipated energy in a dielectric system [37]. The frequency dependence of $tan\delta$ for all samples is depicted in **Fig. 15**. The relaxation peak noticed for each $tan\delta(f)$ plot appears when jumping frequency of the localized charge carriers becomes approximately equal to that of external electric field

[89]. The low dielectric loss values at higher frequencies (inset of **Fig. 15**) make the synthesized NPs suitable materials for high frequency applications.

3.6.2. ac conductivity

The ac conductivity (σ_{ac}) of a dielectric material can be calculated using the following relation [37]:

$$\sigma_{ac} = \varepsilon' \varepsilon_0 \omega \, tan\delta \tag{15}$$

where ω is the angular frequency ($\omega = 2\pi f$).

The $\sigma_{ac}(f)$ plots of undoped, Al and (Al+Mn) doped ZnO samples are displayed in **Fig. 16**. The observed slow increase in conductivity at low frequencies becomes rapid at higher ones for all samples. At low frequencies, few charge carriers tunnel through the potential barrier that forms the grain boundaries, giving rise to a feeble conductivity. The more charge carriers tunneling with increasing frequency enhances conductivity. Beyond a certain frequency, charge carriers get sufficient energy to overcome the potential barrier leading to a rapid increase in conductivity at higher frequencies [89,90]. It is clearly seen from **Fig. 16** that conductivity increases due to doping and with increasing Mn content up to 2% but decreases for 3%. The charge carrier density induced by addition of dopants may be the possible reason for the observed increase in conductivity [89,91]. Besides the charge carrier creation, doping induces in the ZnO host lattice defects like zinc interstitials and oxygen vacancies [86,92] which tend to segregate at the grain boundaries. Doping induced defect ions facilitate the formation of grain boundary defect barrier leading to blockage of charge carriers flow [92] which in turn decreases conductivity [37,86].

These plots of **Fig. 16** are fitted according to the Jonscher's power law [93]:

$$\sigma_{ac}(\omega) = \sigma_{dc} + B\omega^s \tag{16}$$

where σ_{dc} is the dc conductivity, B is a constant and s is an exponent ($0 \leq s \leq 1$).

The s values extracted from drawn fits lie between 0.65 and 0.95 (inset of **Fig. 16**), which suggests that the conduction is governed by the hopping mechanism in all nanopowders.

3.6.3. Impedance spectroscopy

Variations of the real part (Z') of complex impedance with frequency for undoped, Al and (Al+Mn) doped ZnO nanopowders are displayed in **Fig. 17a.** The higher Z' values are noticed at low frequency region which corresponds to high resistivity due to effectiveness of resistive grain boundaries at this frequency range **[16,63]**. The observed decrement in Z' with increasing frequency may be due to the ac conductivity increase with the rise in frequency **[63]**. **Fig. 17b**. shows the frequency dependence of the imaginary part (Z'') of complex impedance for all samples. Each $Z''(f)$ plot exhibits a relaxation peak which decreases in intensity due to doping indicating a loss decrease in the doped NPs **[94]**.

The Cole-Cole plots of all nanopowders are given in **Fig. 18**. A single depressed semicircle is observed for each sample. Its center lying below the Z' axis shows a non-Debye relaxation **[93]**. The equivalent electrical circuit for all samples is a parallel combination of resistance R_b (bulk resistance) and a constant phase element (CPE) as found for undoped and Na doped ZnO nanoparticles **[93]**. The impedance of CPE is given by **[95]**:

$$Z_{CPE}^* = \frac{1}{Q(j\omega)^\alpha}$$
(17)

where j is the imaginary unit $(j^2 = -1)$, Q is a constant in $F.cm^{-2}.s^{\alpha-1}$ **[96]** and α is a dimensionless parameter ranging between zero and unity and determining the degree of deviation from an exact semicircle.

$Z'(f)$ and $Z''(f)$ plots (**Figs. 17a** and **17b**) were fitted using the following relations **[95]**:

$$Z' = \frac{R_b\left(1+R_bQ\omega^\alpha\cos\left(\frac{\alpha\pi}{2}\right)\right)}{1+2R_bQ\omega^\alpha\cos\left(\frac{\alpha\pi}{2}\right)+(R_bQ\omega^\alpha)^2}$$
(18)

$$Z'' = \frac{R_b^2Q\omega^\alpha\sin\left(\frac{\alpha\pi}{2}\right)}{1+2R_bQ\omega^\alpha\cos\left(\frac{\alpha\pi}{2}\right)+(R_bQ\omega^\alpha)^2}$$
(19)

Furthermore, all semicircles were fitted on the basis of these relationships (**Fig. 18**). As shown in this figure, there is a good accordance between experimental data and fits, which indicates that the proposed equivalent circuit is a suitable one for characterizing the electrical behavior of samples. The extract parameters for the circuit elements are gathered in **table 4**. It is clearly seen that the resistance R_b decreases due to doping and with increasing Mn content up to 2% and increases for 3%, which is consistent with conductivity variation.

4. Conclusion

Undoped, Al and (Al+Mn) doped ZnO nanopowders with a constant Al content of 3% and different Mn contents (1%, 2% and 3%) were successfully synthesized by the low cost effective co-precipitation method. All nanopowders crystallize in hexagonal wurtzite structure without any secondary phase. Both single and double doping induce an increase of crystallite size average and a decrease of micro-strain and dislocation density. The variation of average crystallite size was found to be Mn content dependent. The improvement of optical transparency in the visible range due to single or double doping can be related to the grain boundaries decrease which in turn could reduce the light scattering. For all doped samples, the Urbach energy increases as compared to undoped one suggesting an increase in disorder and defects amount. The optical band gap decreases due to doping whatever its type and with increasing Mn content up to 2% but slightly increases for 3%. The E_g red shift was related to defects creation and the average crystallite size increase while E_g blue shift was interpreted based on Burstein-Moss effect. All PL spectra exhibit two emission peaks in UV and visible regions. The deconvolution of the visible emission peak using a Gaussian analysis reveals different emissions for all nanopowders. More emissions are noticed for (Al+Mn) doped samples, which suggests an enhancement of luminescence properties of ZnO in the visible spectral range due to incorporation of aluminum and manganese. An increase in ac conductivity (σ_{ac}) was observed for all doped samples and was discussed based on the charge

carrier density induced by doping. Cole-Cole plots of all nanopowders were suitably fitted to a circuit consisting in a parallel combination of a resistance and a constant phase element (CPE). On the basis on results of the present work, we suggest that (Al+Mn) doping can enhance the optical and conducting properties of ZnO, which may meet the requirements for an improvement of the optoelectrical efficiency of solar cells.

References

[1] P. Liang, H. Cai, X. Yang, H. Li, W. Zhang, N. Xu, J. Sun, J. Wu, Spectroscopic characterization of the plasmas formed during the deposition of ZnO and Al-doped ZnO films by plasma-assisted pulsed laser deposition, Spectrochim. Acta Part B 125 (2016) 18–24.

[2] R. Sangeetha, S. Muthukumaran, M. Ashokkumar, Structural, optical, dielectric and antibacterial studies of Mn doped $Zn_{0.96}Cu_{0.04}O$ nanoparticles, Spectrochim. Acta A Mol. Biomol. Spectrosc. 144 (2015) 1–7.

[3] K. Karthika, K. Ravichandran, Tuning the microstructural and magnetic properties of ZnO nanopowders through the simultaneous doping of Mn and Ni for biomedical applications, J. Mater. Sci. Technol. 31 (2015) 1111–1117.

[4] V.S. Sangawar, M.C. Golchha, Thermally stimulated discharge conductivity study of zinc oxide thermoelectrets, Bull. Mater. Sci. 37 (2014)1497–1501.

[5] K.Assaker, B.Lebeau, L.Michelin, ,P.Gaudin, C.Carteret, L.Vidal, M.Bonne, J.L.Blin, J. Alloys Comp. 649 (2015) 190-195.

[6] DaChen, ZhongyingXue, XingWei, GangWang, LinYe, MiaoZhang, DewangWang, SuLiu, Appl. Surf. Sci. 299 (2014) 12-18.

[7] A.N. El-Shazly, M.M. Rashad, E.A. Abdel-Aal, I.A. Ibrahim, M.F. El-Shahat, A.E. Shalan, Nanostructured ZnO photocatalysts prepared via surfactant assisted co-precipitation method achieving enhanced photocatalytic activity for the degradation of methylene blue dyes, J. Environ. Chem. Eng. 4 (2016) 3177–3184.

[8] G.K. Mani, J.B.B. Rayappan, Facile synthesis of ZnO nanostructures by spray pyrolysis technique and its application as highly selective H_2S sensor, Mater. Lett. 158 (2015) 373–376.

[9] J. Ungula, B.F. Dejene, Effect of solvent medium on the structural, morphological and optical properties of ZnO nanoparticles synthesized by the sol-gel method, Physica B: Condens. Matter 480 (2016) 26–30.

[10] V.E. Sandana, D.J. Rogers, F.H. Teherani, R. McClintock, C. Bayram, M. Razeghi, H.J. Drouhin, M.C. Clochard, V. Sallet, G. Garry, F. Falyouni, Comparison of ZnO nanostructures grown using pulsed laser deposition, metal organic chemical vapor deposition, and physical vapor transport, J. Vac. Sci. Technol. B 27 (2009) 1678–1683.

[11] S.M. Saleh, A.M. Soliman, M.A. Sharaf, V. Kale, B. Gadgil, Influence of solvent in the synthesis of nano-structured ZnO by hydrothermal method and their application in solar-still, J. Environ. Chem. Eng. 5 (2017) 1219–1226.

[12] WeiZhang, MengLi, XuezhangXiao, XuHuang, YiqunJiang, XiulinFan, LixinChen, Journal of Alloys and Compounds 727 (2017) 792-820.

[13] Hong-YiLi, Xin Qiu, Meng Dong, Xinlu Li, Yuxin Zhang, Bing Xie, Ceram. Int. 41(2015) 13983-13987.

[14] Oluwamayowa O.Adigun, Alexander S.Freer, Jeffrey T.Miller, L. SueLoesch-Fries, Bong SukKim, Michael T.Harris, Journal of Colloid and Interface Science 450 (2015) 381–387.

[15] M. Shatnawi, A.M Alsmadi, I. Bsoul, B. Salameh, M. Mathai, G. Alnawashi, G.M. Alzoubi, F. Al-Dweri, M.S. Bawa'aneh, Influence of Mn doping on the magnetic and optical properties of ZnO nanocrystalline particles, Results Phys. 6 (2016) 1064–1071.

[16] M. Arshad, A.S. Ahmed, A. Azama, A.H. Naqvi, Exploring the dielectric behavior of Co doped ZnO nanoparticles synthesized by wet chemical route using impedance spectroscopy, J. Alloys Compd. 577 (2013) 469–474.

[17] I.Y. Kim, S.W. Shin, M.G. Gang, S.H. Lee, K.V. Gurav, P.S. Patil, J.H. Yun, J.Y. Lee, J. H. Kim,Comparative study of quaternary Mg and Group III element co-doped ZnO thin films with transparent conductive characteristics 570 (2014) 321-325.

[18] P. Li, S. Wang, J. Li, Y. Wei, Structural and optical properties of Co-doped ZnO nanocrystallites prepared by a one-step solution route, J. Lumin. 132 (2012) 220–225.

[19] G. El Hallani, S. Nasih, N. Fazouan, A. Liba, M. Khuili, M. Sajieddine, M. Mabrouki, L. Laanab, E.H. Atmani, Comparative study for highly Al and Mg doped ZnO thin films elaborated by sol gel method for photovoltaic application, J. Appl. Phys. 121 (2017) 135103-1– 135103-7.

[20] K. Karthika, K. Ravichandran, Enhancing the magnetic and antibacterial properties of ZnO nanopowders through Mn+Co doping, Ceram. Int. 41 (2015) 7944–7951.

[21] V.D. Mote, J.S. Dargad, B.N. Dole, Effect of Mn doping concentration on structural, morphological and optical studies of ZnO nano-particles, Nanosci. Nanoeng. 1 (2013) 116–122.

[22] K. Ravichandran, K. Karthika, B. Sakthivel, N. Jabena Begum, S. Snega, K. Swaminathan, V. Senthamilselvi, Tuning the combined magnetic and antibacterial properties of ZnO nanopowders through Mn doping for biomedical applications, J. Magn. Magn. Mater. 358-359 (2014) 50–55.

[23] S. Fabbiyola, L.J. Kennedy, A.A. Dakhel, M. Bououdina, J.J. Vijaya, T. Ratnaji, Structural, microstructural, optical and magnetic properties of Mn-doped ZnO nanostructures, J. Mol. Struct. 1109 (2016) 89–96.

[24] A.N. Mallika, A. Ramachandra Reddy, K. Sowribabu, K.Venugopal Reddy, Structural and optical characterization of $Zn_{0.95\_x}Mg_{0.05}Al_xO$ nanoparticles, Ceram. Int. 41 (2015) 9276–9284.

[25] M. Kahouli, A. Barhoumi, A. Bouzid, A. Al-Hajry, S. Guermazi, Structural and optical properties of ZnO nanoparticles prepared by direct precipitation method, Superlattices Microstruct. 85 (2015) 7–23.

[26] G. Vijayaprasath, R. Murugan, S. Asaithambi, G. Anandha Babu, P. Sakthivel, T. Mahalingam, Y. Hayakawa, G. Ravi, Structural characterization and magnetic properties of Co co-doped Ni/ZnO nanoparticles, Appl. Phys. A 122 (2016) 1–11.

[27] T. Coman, E.L. Ursu, V. Nica, V. Tiron, M. Olaru, C. Cotofana, M. Dobromir, A. Coroaba, O.G. Dragos, N. Lupu, O.F. Caltun, C. Ursu, Improving the uncommon (110) growing orientation of Al-doped ZnO thin films through sequential pulsed laser deposition, Thin Solid Films 571 (2014) 198–205.

[28] G. Kaur, A Mitra, K.L. Yadav, Pulsed laser deposited Al-doped ZnO thin films for optical applications, Prog. Nat. Sci. Mater. Int. 25 (2015) 12–21.

[29] V.D. Mote, J.S. Dargad, Y. Purushotham, B.N. Dole, Effect of doping on structural, physical, morphological and optical properties of $Zn_{1-x}Mn_xO$ nano-particles, Ceram. Int. 41 (2015) 15153–15161.

[30] M. Yilmaz, G. Turgut, Titanium doping effect on the characteristic properties of sol-gel deposited ZnO thin films, Kovove Mater. 53 (2015) 333–339.

[31] S. Snega, K. Ravichandran, M. Baneto, S. Vijayakumar, Simultaneous enhancement of transparent and antibacterial properties of ZnO films by suitable F doping, J. Mater. Sci. Technol. 31 (2015) 759–765.

[32] C. Mrabet, O. Kamoun, A. Boukhachem, M. Amlouk, T. Manoubi, Some physical investigations on hexagonal-shaped nanorods of lanthanum-doped ZnO, J. Alloys Compd. 648 (2015) 826–837.

[33] A.J. Reddy, M.K. Kokila, H. Nagabhushana, R.P.S. Chakradhar, C. Shivakumara, J.L. Rao, B.M. Nagabhushana, Structural, optical and EPR studies on ZnO:Cu nanopowders prepared via low temperature solution combustion synthesis, J. Alloys Compd. 509 (2011) 5349–5355.

[34] T. Srinivasulu, K. Saritha, K.T. Ramakrishna Reddy, Synthesis and characterization of Fe-doped ZnO thin films deposited by chemical spray pyrolysis, Mod. Electron. Mater. 3 (2017) 76–85.

[35] C.H. Wömer, P.M. Hazzledine, Grain growth stagnation by inclusions or pores, JOM 44 (1992) 16–20.

[36] A.T. Ravichandran, K. Catherine Siriya Pushpa, K. Ravichandran, K. Karthika, B.M. Nagabhushana, S. Mantha, K. Swaminathan, Effect of Al doping on the structural and optical properties of ZrO_2 nanopowders synthesized using solution combustion method, Superlattices Microstruct. 75 (2014) 533–542.

[37] M. Mehedi Hassan, W. Khan, A. Azam, A.H. Naqvi, Influence of Cr incorporation on structural, dielectric and optical properties of ZnO nanoparticles, J. Ind. Eng. Chem. 21 (2015) 283–291.

[38] J.J. Beltrán, C.A. Barrero, A. Punnoose, Identifying the sources of ferromagnetism in sol-gel synthesized $Zn_{1-x}Co_xO$ ($0 \leq x \leq 0.10$) nanoparticles, J. Solid State Chem. 240 (2016) 30–42.

[39] D. Anbuselvan, S. Muthukumaran, Defect related microstructure, optical and photoluminescence behaviour of Ni, Cu co-doped ZnO nanoparticles by co-precipitation method, Opt. Mater. 42 (2015) 124–131.

[40] D. Guruvammal, S. Selvaraj, S.M. Sundar, Effect of Ni-doping on the structural, optical and magnetic properties of ZnO nanoparticles by solvothermal method, J. Alloys Compd. 682 (2016) 850–855.

[41] M. Gharagozlou, S. Naghibi, Sensitization of ZnO nanoparticle by vitamin B_{12}: investigation of microstructure, FTIR and optical properties, Mater. Res. Bull. 84 (2016) 71–78.

[42] M. Gharagozlou, Z. Baradaran, R. Bayati, A green chemical method for synthesis of ZnO nanoparticles from solid-state decomposition of Schiff-bases derived from amino acid alanine complexes, Ceram. Int. 41 (2015) 8382–8387.

[43] S. Dutta, B.N. Ganguly, Characterization of ZnO nanoparticles grown in presence of folic acid template, J. Nanobiotechnology 10 (2012) 1–10.

[44] R.N. Aljawfi, F. Rahman, K.M. Batoo, Surface defect mediated magnetic interactions and ferromagnetism in Cr/Co Co-doped ZnO nanoparticles, J. Magn. Magn. Mater. 332 (2013) 130–136.

[45] V. Pazhanivelu, A.P.B. Selvadurai, R. Kannan, R. Murugaraj, Room temperature ferromagnetism in Ist group elements codoped ZnO:Fe nanoparticles by co-precipitation method, Physica B: Condens. Matter 487 (2016) 102–108.

[46] B. Pal and P.K. Giri, High temperature ferromagnetism and optical properties of Co doped ZnO nanoparticles, J. Appl. Phys. 108 (2010) 084322-1– 084322-8.

[47] A. Umar, S.H. Kim, Y.S. Lee, K.S. Nahm, Y.B. Hahn, Catalyst-free large-quantity synthesis of ZnO nanorods by a vapor-solid growth mechanism: structural and optical properties, J. Cryst. Growth 282 (2005) 131–136.

[48] F. Decremps, J. Pellicer-Porres, A.M. Saitta, J.C. Chervin, A. Polian, High-pressure Raman spectroscopy study of wurtzite ZnO, Phys. Rev. B 65 (2002) 092101-1–092101-4.

[49] S. Jabri, G. Amiri, S. Hassani, A. Lusson, V. Sallet, A. Meftah, P. Galtier, M. Oueslati, Zinc blende-oxide phase transformation upon oxygen annealing of ZnSe shell in ZnO-ZnSe core-shell nanowires, Appl. Phys. Lett. 110 (2017) 101601-1–101601-5.

[50] A. Abdel-Galil, M.R. Balboul, A. Sharaf, Synthesis and characterization of Mn-doped ZnO diluted magnetic semiconductors, Physica B 477 (2015) 20–28.

[51] T. Jan, J. Iqbal, M. Ismail, Q. Mansoor, A. Mahmood, A. Ahmad, Eradication of multi-drug resistant Bacteria by Ni doped ZnO nanorods: structural, Raman and optical characteristics, Appl. Surf. Sci. 308 (2014) 75–81.

[52] Q. Gao, Y. Dai, C. Li, L. Yang, X. Li, C. Cui, Correlation between oxygen vacancies and dopant concentration in Mn-doped ZnO nanoparticles synthesized by co-precipitation technique, J. Alloys Compd. 684 (2016) 669–676.

[53] X. Wang, J. Xu, B. Zhang, H. Yu, J. Wang, X. Zhang, J. Yu, Q. Li, Signature of intrinsic high temperature ferromagnetism in cobalt doped zinc oxide nanocrystals, Adv. Mater. 18 (2006) 2476–2480

[54] J. Das, D.K. Mishra, V.V. Srinivasu, D.R. Sahu, B.K. Roul, Photoluminescence and Raman studies for the confirmation of oxygen vacancies to induce ferromagnetism in Fe doped Mn:ZnO compound, J. Magn. Magn. Mater. 382 (2015) 111–116.

[55] A.K. Pradhan, K. Zhang, G.B. Loutts, U.N. Roy, Y. Cui, A. Burger, Structural and spectroscopic characteristics of ZnO and ZnO:Er^{3+} nanostructures, J. Phys.: Condens. Matter 16 (2004) 7123–7129.

[56] S. Das, S. Das, S. Sutradhar, Enhanced dielectric behavior and ac electrical response in Gd-Mn-ZnO nanoparticles, J. Alloys Compd. 726 (2017) 11–21.

[57] V. Pazhanivelu, A.P.B. Selvadurai, Y. Zhao, R. Thiyagarajan, R. Murugaraj, Room temperature ferromagnetism in Mn doped ZnO: Co nanoparticles by co-precipitation method, Physica B: Condens. Matter 481 (2016) 91–96.

[58] H. Zhang, S. Qin, Y. Cao, Z. Yang, L. Si, W. Zhong, D. Wu, M. Xu, Q. Xu, Enhanced room temperature ferromagnetism in hydrogenated $Zn_{0.98}Mn_{0.02}O$, Appl. Surf. Sci. 271 (2013) 421– 423.

[59] C.X. Xu, X.W. Suna, Z.L. Dong, S.T. Tan, Y.P. Cui, B.P. Wang, Manganese-doped zinc oxide tetratubes and their photoluminescent properties, J. Appl.Phys. 98 (2005) 113513-1– 113513-5.

[60] L. Wang, L. Meng, V. Teixeira, S. Song, Z. Xu, X. Xu, Structure and optical properties of ZnO:V thin films with different doping concentrations, Thin Solid Films 517 (2009) 3721–3725.

[61] A. Davoodi, M. Tajally, O. Mirzaee, A. Eshaghi, The effects of Ti concentration on the structure, optical, and electrical properties of Al and Ti co-doped ZnO thin films, Optik 127 (2016) 4645–4649.

[62] R. Mimouni, O. Kamoun, A. Yumak, A. Mhamdi, K. Boubaker, P. Petkova, M. Amlouk, Effect of Mn content on structural, optical, opto-thermal and electrical properties of ZnO:Mn sprayed thin films compounds, J. Alloys Compd. 645 (2015) 100–111.

[63] S.A. Ansari, A. Nisar, B. Fatma, W. Khan, A.H. Naqvi, Investigation on structural, optical and dielectric properties of Co doped ZnO nanoparticles synthesized by gel-combustion route, Mater. Sci. Eng. B 177 (2012) 428– 435.

[64] A. Bedia, F.Z. Bedia, M. Aillerie, N. Maloufi, B. Benyoucef, Morphological and optical properties of ZnO thin films prepared by spray pyrolysis on glass substrates at various temperatures for integration in solar cell, Energy Procedia 74 (2015) 529–538.

[65] O. Makuku, F. Mbaiwa, T.S. Sathiaraj, Structural, optical and electrical properties of low temperature grown undoped and (Al, Ga) co-doped ZnO thin films by spray pyrolysis, Ceram. Int. 42 (2016) 14581–14586.

[66] M. Nafees, W. Liaqut, S. Ali, M.A. Shafique, Synthesis of ZnO/Al:ZnO nanomaterial: structural and band gap variation in ZnO nanomaterial by Al doping, Appl. Nanosci. 3 (2013) 49–55.

[67] M. Ahmad, E. Ahmed, Y. Zhang, N.R. Khalid, J. Xu, M. Ullah, Z. Hong, Preparation of highly efficient Al-doped ZnO photocatalyst by combustion synthesis, Curr. Appl. Phys. 13 (2013) 697–704.

[68] S. El Yamny, M. Abdel Rafea, Preparation and characterization of ZnO:In transparent conductor by low cost dip coating technique, J. Mod. Phys. 3 (2012) 1060-1069.

[69] Transition metal (Co, Mn) co-doped ZnO nanoparticles: Effect on structural and optical properties, J. Alloys Compd. 698 (2015) 532–538.

[70] R.B. Bylsma, M. Becker, J. Kossut, U. Debska, Dependence of energy gap on x and T in $Znt_{1-x}Mn_x$ Se: the role of exchange interaction, Phys. Rev. B 33 (1986) 8207-8215.

[71] R. Joshi, P. Kumar, A. Gaur, K. Asokan, Structural, optical and ferroelectric properties of V doped ZnO, Appl. Nanosci. 4 (2014) 531–536.

[72] H.A. Hussin, Effect of Al dopants on the optical and dispersion parameters of iron oxide thin films, Int. J. Sci. Res. Sci. Technol. 2 (2016) 232–235.

[73] D.P. Gupta, S. Kumar, P.C. Kalsi, V.K. Manchanda, V.K. Mittal, γ-ray modifications of optical/chemical properties of polycarbonate polymer, World J. Condens. Matter Phys. 5 (2015) 129–137.

[74] O MEGLALI, N ATTAF, A BOURAIOU, M S AIDA and S LAKEHAL, One-step electrodeposition process of CuInSe2: Deposition time effect, Bull. Mater. Sci., 37 (2014), 1535–1542.

[75] Zahid Rizwan, Azmi Zakaria, Mohd Sabri Mohd Ghazali, Atefeh Jafari, Fasih Ud Din and Reza Zamiri, Effect of Annealing Temperature on the Optical Spectra of CdS Thin Films Deposited at Low Solution Concentrations by Chemical Bath Deposition (CBD) Technique, Int. J. Mol. Sci, 12 (2011) 1293-1305.

[76] D. Fang, P. Yao, H. Li, Influence of annealing temperature on the structural and optical properties of Mg-Al co-doped ZnO thin films prepared via sol–gel method, Ceram. Int. 40 (2014) 5873–5880.

[77] K. Uchida, T. Ota, H. Adachi, J. Xiao, T. Nonaka, Y. Kajiwara, G. E. W. Bauer, S. Maekawa, and E. Saitoh, Journal of Applied Physics, 111 (2012) 1488.

[78] J. K. Tripathi, G. Markovich, and I. Goldfarb, Applied Physics Letters, 102 (2013) 1488.

[79] Y.M. Hao, S.Y. Lou, S.M. Zhou, R.J. Yuan, G.Y. Zhu, N. Li, Structural, optical, and magnetic studies of manganese-doped zinc oxide hierarchical microspheres by self-assembly of nanoparticles, Nanoscale Res. Lett. 7 (2012) 1–9.

[80] S. Fabbiyola, V. Sailaja, L.J. Kennedy, M. Bououdina, J.J. Vijaya, Optical and magnetic properties of Ni-doped ZnO nanoparticles, J. Alloys Compd. 694 (2017) 522–531.

[81] Z.J. Yan, D.W. Zeng, C.S. Xie, H.H. Wang, W.L. Song, Nanostructured ZnO network films deposited on Al_2O_3 substrates by chemical bath deposition, Thin Solid Films 517 (2009) 1541–1545.

[82] H.S. Kang, J.W. Kim, S.H. Lim, H.W. Chang, G.H. Kim, J.H. Kim, S.Y. Lee, Investigation on the variation of green, yellow, and orange emission properties of ZnO thin film, Superlattices Microstruct. 39 (2006) 193–201.

[83] R. Amiruddin, M.C. Santhosh Kumar, Enhanced visible emission from vertically aligned ZnO nanostructures by aqueous chemical growth process, J. Lumin. 155 (2014) 149–155.

[84] T. Prodromakis, C. Papavassiliou, Engineering the Maxwell–Wagner polarization effect, Appl. Surf. Sci. 255 (2009) 6989–6994.

[85] C.G. Koops, On the dispersion of resistivity and dielectric constant of some semiconductors at audiofrequencies, Phys. Rev. 83 (1951) 121–124.

[86] R. Zamiri, A. Kaushal, A. Rebelo, J.M.F. Ferreira, Er doped ZnO nanoplates: synthesis, optical and dielectric properties, Ceram. Int. 40 (2014) 1635–1639.

[87] M. Ashokkumar, S. Muthukumaran, Effect of Cr-doping on dielectric, electric and magnetic properties of $Zn_{0.96}Cu_{0.04}O$ nanopowders, Powder Technol. 268 (2014) 80–85.

[88] R. Zamiri, B. Singh, I. Bdikin, A. Rebelo, M. S. Belsley, J.M.F. Ferreira, Influence of Mg doping on dielectric and optical properties of ZnO nano-plates prepared by wet chemical method, Solid State Commun. 195 (2014) 74–79.

[89] M. Ashokkumar, S. Muthukumaran, Electrical, dielectric, photoluminescence and magnetic properties of ZnO nanoparticles co-doped with Co and Cu, J. Magn. Magn. Mater. 374 (2015) 61–66.

[90] M. Ashokkumar, S. Muthukumaran, Effect of Ni doping on electrical, photoluminescence and magnetic behavior of Cu doped ZnO nanoparticles. J. Lumin. 162 (2015) 97–103.

[91] R. Zamiri, B. Singh, M.S. Belsley, J.M.F. Ferreira, Structural and dielectric properties of Al-doped ZnO nanostructures, Ceram. Int. 40 (2014) 6031–6036.

[92] X. Li, X. Cao, L. Xu, L. Liu, Y. Wang, C. Meng, Z. Wang, High dielectric constant in Al-doped ZnO ceramics using high-pressure treated powders, J. Alloys Compd. 657 (2016) 90–94.

[93] A. Tabib, N. Sdiri, H. Elhouichet, M. Férid, Investigations on electrical conductivity and dielectric properties of Na doped ZnO synthesized from sol gel method, J. Alloys Compd. 622 (2015) 687–694.

[94] A. Azam, A.S. Ahmed, M.S. Ansari, M. Shafeeq M, A.H. Naqvi, Study of electrical properties of nickel doped SnO_2 ceramic nanoparticles, J. Alloys Compd. 506 (2010) 237–242.

[95] N. Sdiri, H. Elhouichet, B. Azeza, F. Mokhtar, Study of (90-x) P_2O_5-XB_2O_3-$10Fe_2O_3$ glasses by Mossbauer effect and impedance spectroscopy methods, J. Non Cryst. Solids 371–372 (2013) 22–27.

[96] J.B. Jorcin, M.E. Orazem, N. Pébère, B. Tribollet, CPE analysis by local electrochemical impedance spectroscopy, Electrochim. Acta 51 (2006) 1473–1479.

Figure caption

Fig. 1. X-ray diffraction patterns of undoped, Al and (Al+Mn) doped ZnO nanopwders.

Fig. 2. Evolution of texture coefficient (TC) for the prominent diffraction peaks of undoped, Al and (Al+Mn) doped ZnO nanopwders.

Fig. 3. Plots of $\beta cos\theta$ versus $4sin\theta$ of undoped, Al and (Al+Mn) doped ZnO nanopwders.

Fig. 4. Variations of strain (ε), dislocation density (δ) and average crystallite size (D) as a function of composition.

Fig.5. SEM micrographs of undoped, Al and (Al+Mn) doped ZnO nanopwders.

Fig. 6. FTIR spectra of undoped, Al and (Al+Mn) doped ZnO nanopwders.

Fig. 7. Raman spectra of undoped, Al and (Al+Mn) doped ZnO nanopwders.

Fig. 8. Absorption spectra of undoped, Al and (Al+Mn) doped ZnO nanopwders.

Fig. 9. Transmission spectra of undoped, Al and (Al+Mn) doped ZnO nanopwders.

Fig. 10. Plots of $(\alpha h\nu)^2$ versus photon energy ($h\nu$) for undoped, Al and (Al+Mn) doped ZnO nanopwders.

Fig. 11. Variations of optical band gap (E_g) and Urbach energy (E_u) as a function of composition.

Fig. 12. PL spectra of undoped, Al and (Al+Mn) doped ZnO nanopwders.

Fig. 13. Deconvoluted PL spectra of (a) ZnO (b) AlMnZ0 (c) AlMnZ1 (d) AlMnZ2 and (e) AlMnZ3 nanopowders.

Fig. 14. Variations of $\varepsilon_r^{'}$ versus frequency of undoped, Al and (Al+Mn) doped ZnO nanopwders.

Fig. 15. Variations of $\tan\delta$ versus frequency for undoped Al and (Al+Mn) doped ZnO nanopwders.

Fig. 16. Variations of ac conductivity versus frequency for undoped, Al and (Al+Mn) doped ZnO nanopwders.

Fig. 17. Variations of real (a) and imaginary (b) parts of complex impedance versus frequency for undoped, Al and (Al+Mn) doped ZnO nanopwders.

Fig. 18. Experimental and theoretical impedance diagrams of undoped, Al and (Al+Mn) doped ZnO nanopwders with the corresponding equivalent circuit (inset).
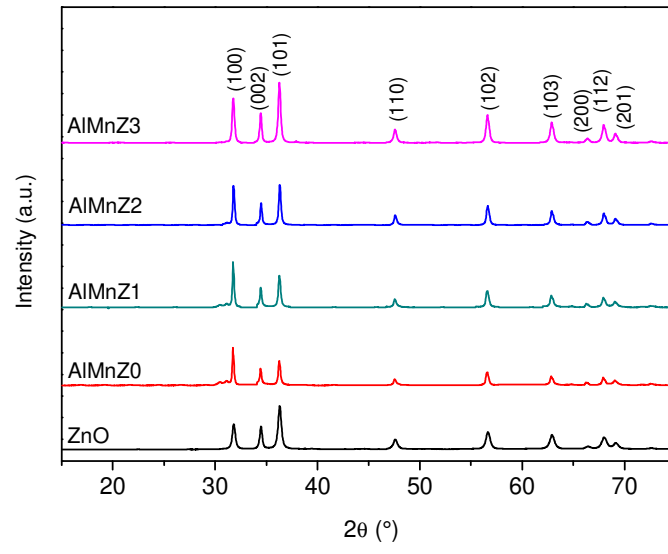
Fig. 1.
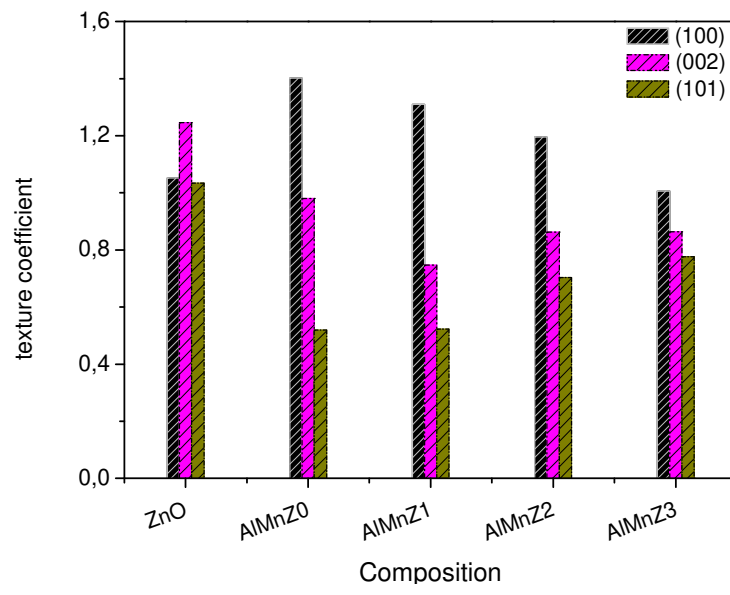
Fig. 2.
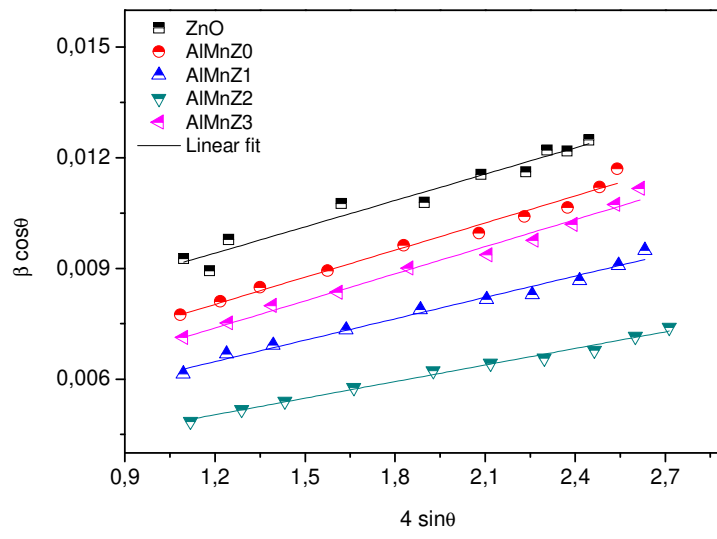
Fig. 3.
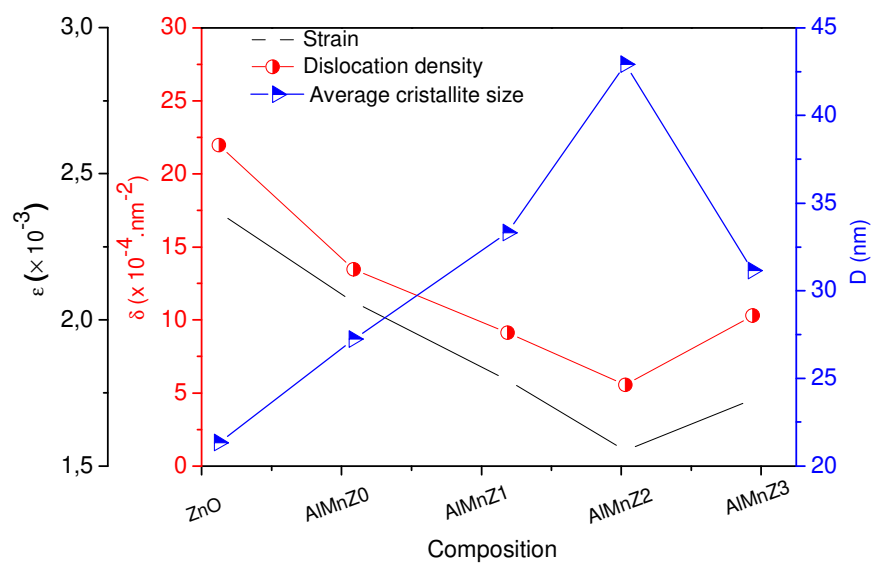
Fig. 4.
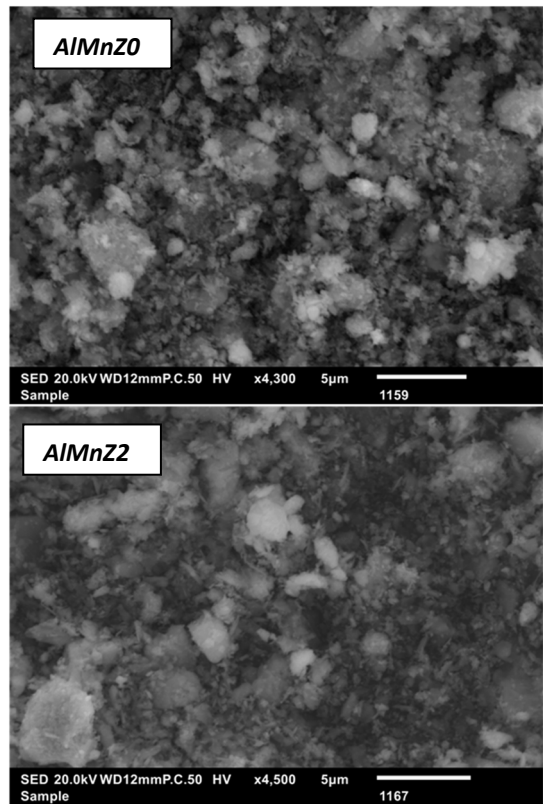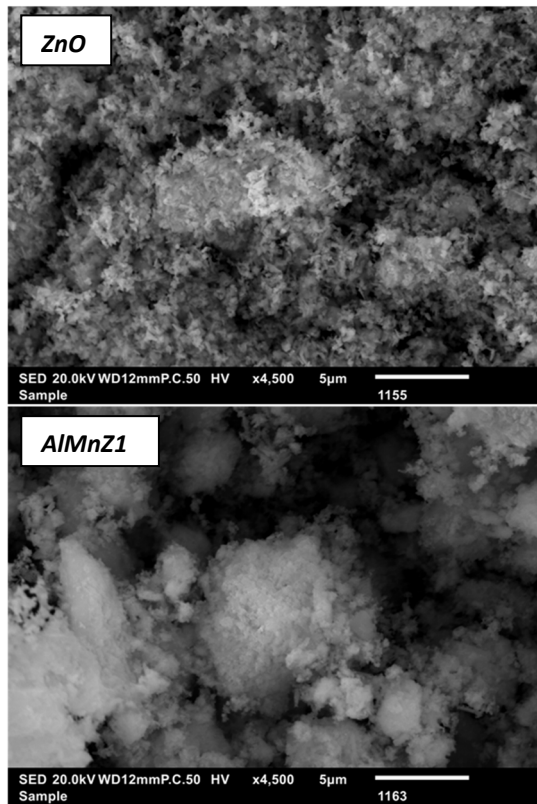
Fig. 5.
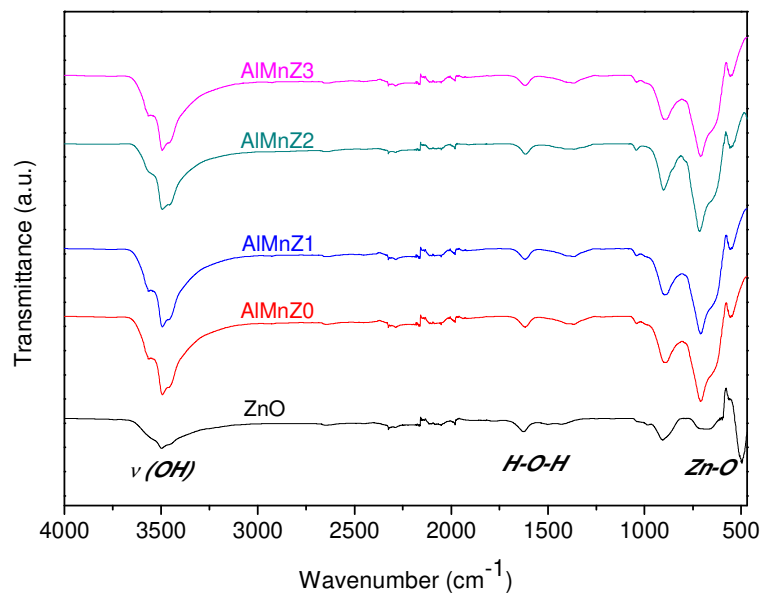
Fig. 6.
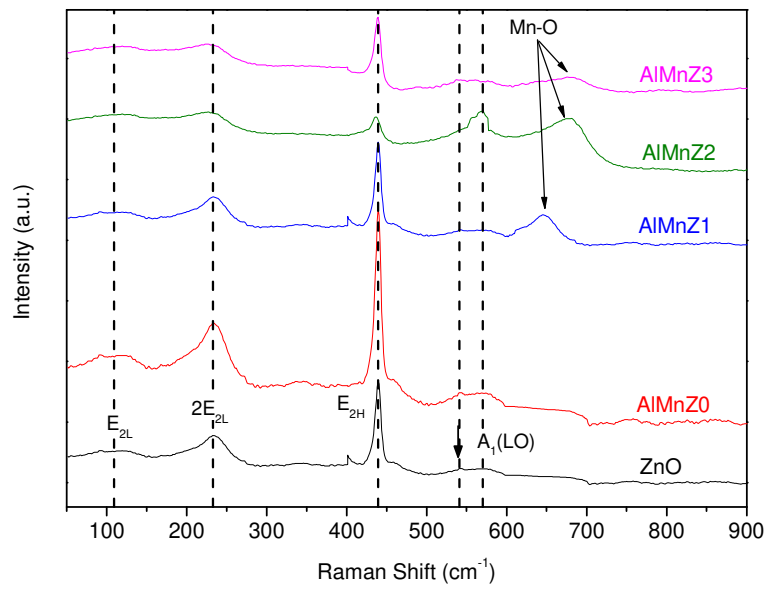
Fig. 7.
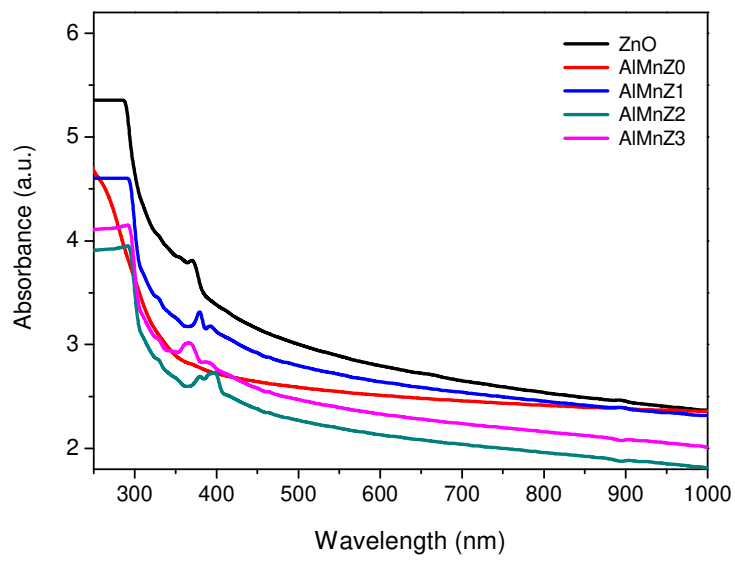
Fig. 8.
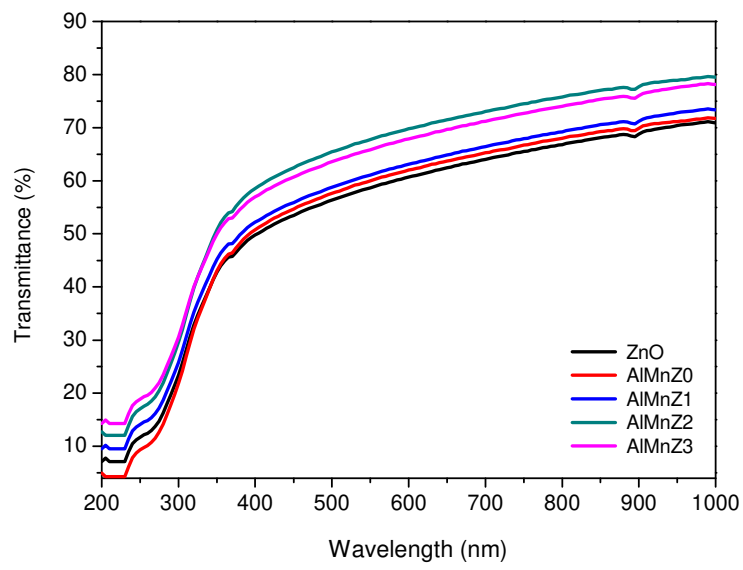
Fig. 9.
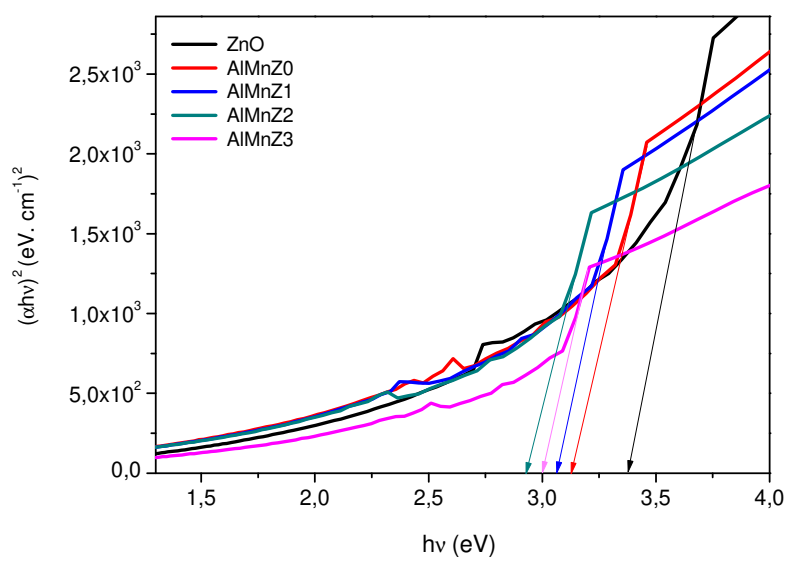
Fig. 10.
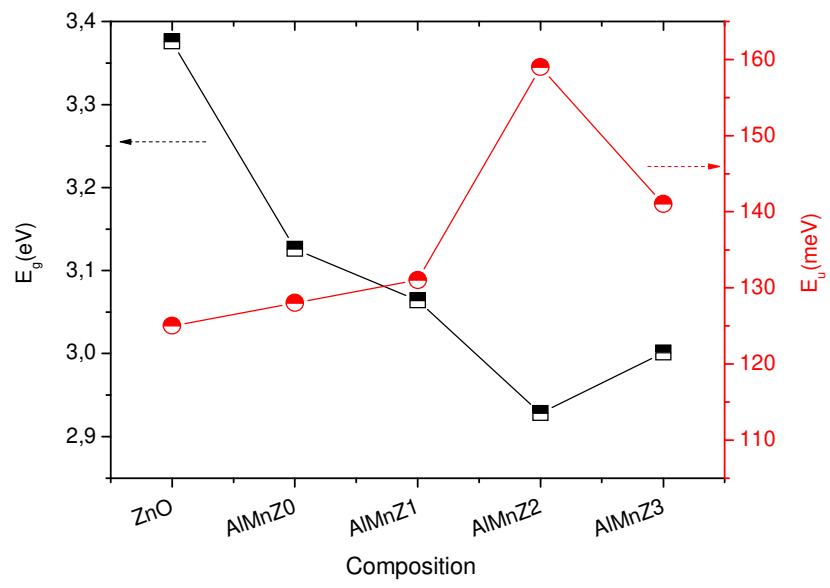
Fig. 11.
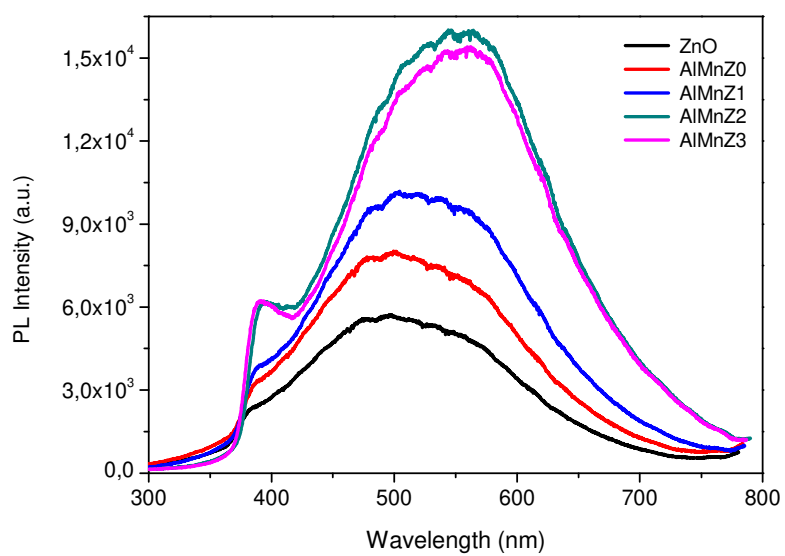
Fig. 12.
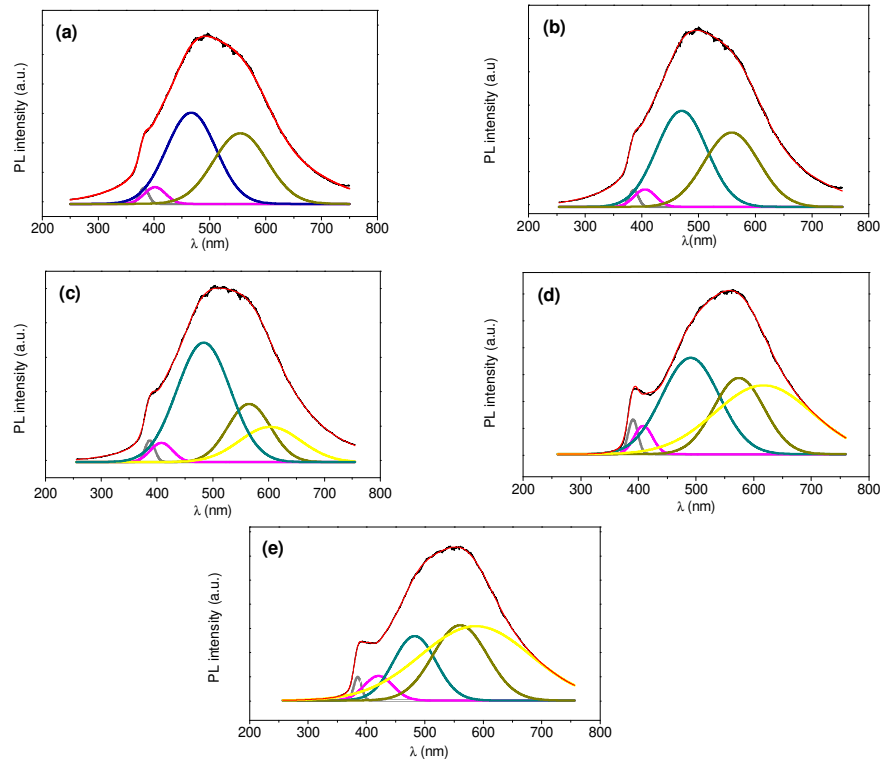
Fig. 13.
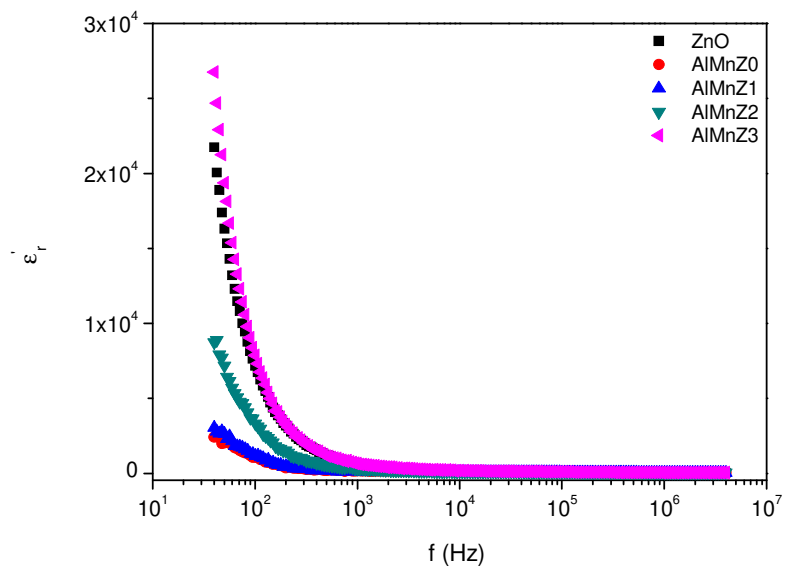
Fig. 14.
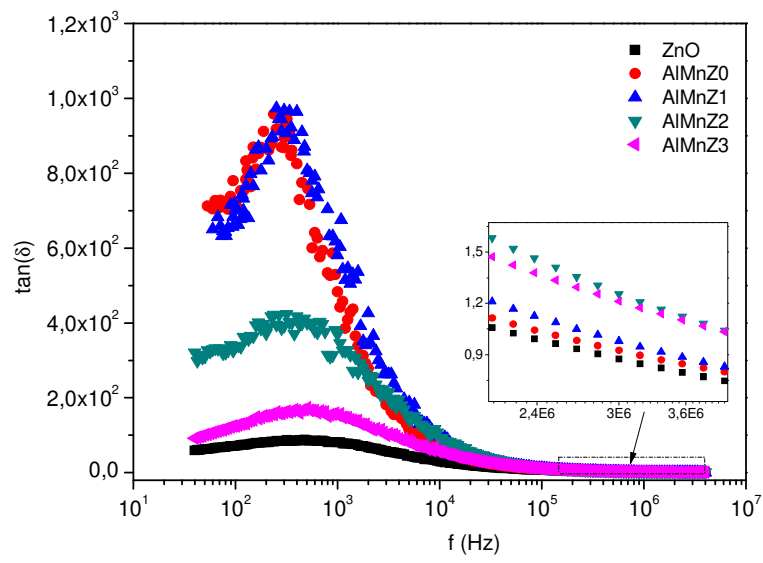
Fig. 15.
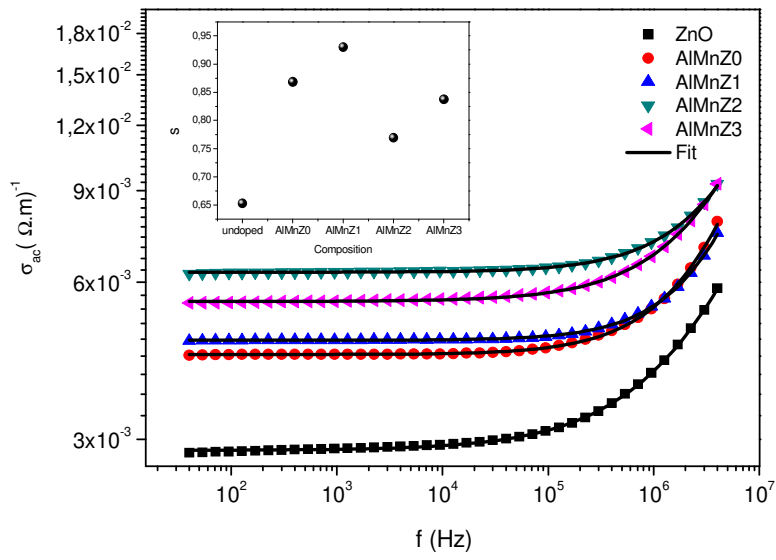
Fig. 16.
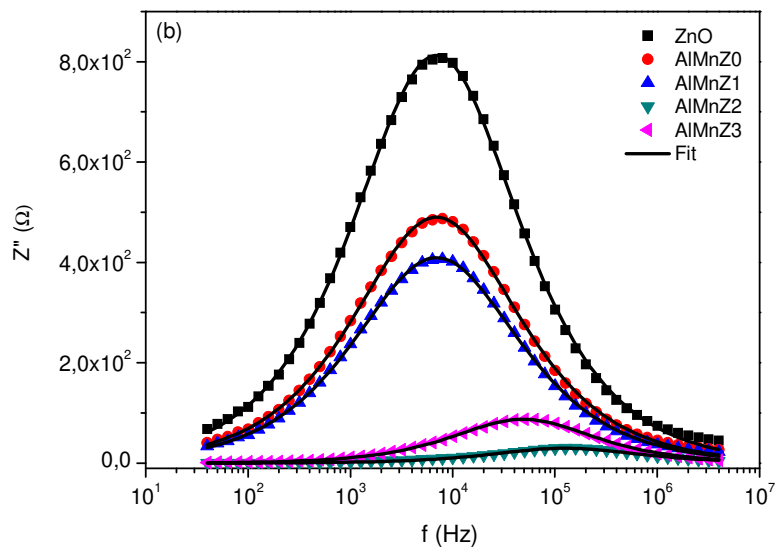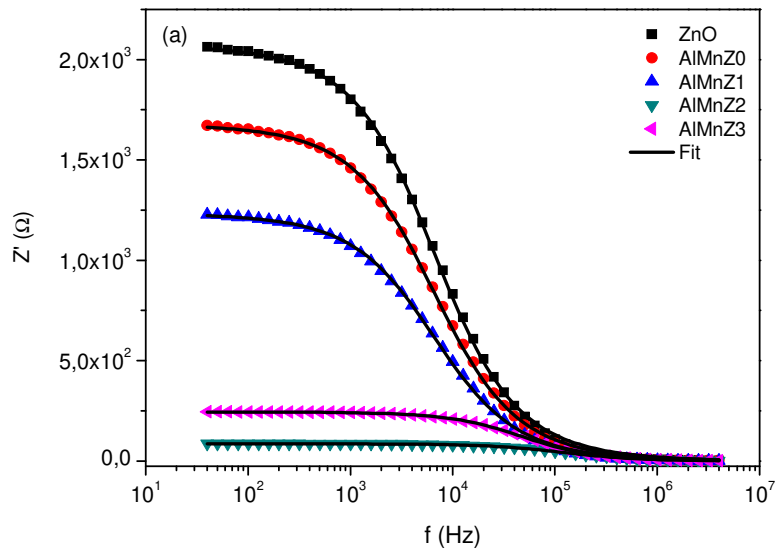
Fig. 17.
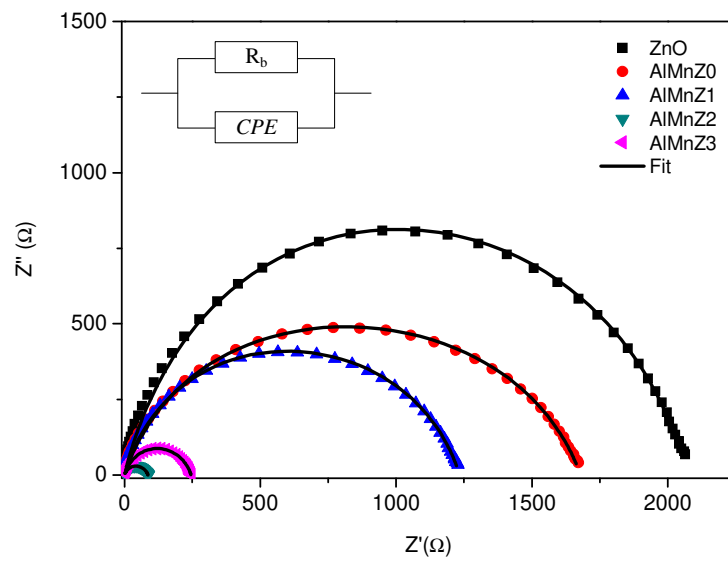
Fig. 18.

Table caption

Table.1 Structural parameters of undoped, Al and (Al+Mn) doped ZnO nanopwders.

Table.2 Calculated values of E_g and E_u

Table.3 Characteristics of photoluminescence peaks: position, energy and Attribution.

Table.4 Fitting values of equivalent circuit elements for different samples

Table.1.

Sample	a ($\mathring{A}$)	c ($\mathring{A}$)	c/a	V ($\mathring{A}^3$)	l ($\mathring{A}$)	$\varepsilon_Z (\times 10^{-3})$	W–H		
							D (nm)	$\varepsilon (\times 10^{-3})$	δ ($\times 10^{-4}$ $line.nm^{-2}$)
ZnO	3,2481	5,2020	1,6015	47,5298	1.9762	-0.8834	21.33±3.38	2.34±0,53	21.97±0,69
AlMnZ0	3.2493	5,2064	1,6023	47.6036	1.9773	-0.0384	27.24±1,25	2.15±0,02	13.47±0,12
AlMnZ1	3.2503	5.2078	1.6022	47.6463	1.9784	0.2304	33.31±0,6	1.93±0,09	9.12±0,35
AlMnZ2	3.2533	5.2093	1.601	47.7471	2.0961	0.5185	42.92±1,35	1.54±0,05	5.54±0,03
AlMnZ3	3.2513	5.2079	1.6017	47.6752	1.9783	0.2496	31.15±1.45	1.71±0.11	10.3±0.09

Table.2.

Sample	E_g (eV)	E_u (eV)
ZnO	3.376	125
AlMnZ0	3.126	128
AlMnZ1	3.064	131
AlMnZ2	2.928	159
AlMnZ3	3.001	141

Table.3

Sample	Peaks	λ (nm)	E (eV)	Attribution
ZnO	1	381.812	3.251	UV
	2	400.754	3.097	Violet
	3	466.456	2.661	Blue
	4	555.233	2.236	Green-yellow
AlMnZ0	1	385.571	3.219	UV
	2	404.513	3.069	Violet
	3	470.215	2.640	Blue-green
	4	558.494	2.222	Green-yellow
AlMnZ1	1	386.452	3.212	UV
	2	407.394	3.047	Violet
	3	483.763	2.566	Blue-green
	4	565.019	2.197	Green-yellow Yellow
	5	604.891	2.052	
AlMnZ2	1	390.094	3.182	UV
	2	409.022	3.035	Violet
	3	486.145	2.553	Blue-green
	4	571.686	2.171	Green-yellow
	5	610.467	2.033	Yellow
AlMnZ3	1	387.213	3.206	UV
	2	404.894	3.066	Violet
	3	481.4189	2.578	Blue-green
	4	560.322	2.215	Green-yellow
	5	589.131	2.107	Yellow

Table.4

Sample	$R_b(\Omega)$	$Q(F)$	a
ZnO	2073.29	1.1310^{-7}	0.74
AlMnZ0	1678.78	1.3910^{-7}	0.74
AlMnZ1	1234.23	1.9010^{-7}	0.74
AlMnZ2	86.70	2.2910^{-7}	0.76
AlMnZ3	245.06	1.2910^{-7}	0.79